

Non peer-reviewed preprint submitted to Proceedings of the National Academy of Sciences

Predictability of abrupt northern-hemisphere cooling events during the last glacial

Takahito Mitsui^{1,2} and Niklas Boers^{1,2,3}

¹Earth System Modelling, School of Engineering & Design, Technical University of Munich

²Potsdam Institute for Climate Impact Research, Telegraphenberg A31, Potsdam, 14473

³Department of Mathematics and Global Systems Institute, University of Exeter

Correspondence: takahito321@gmail.com

Predictability of abrupt northern-hemisphere cooling events during the last glacial

Takahito Mitsui^{1,2}, Niklas Boers^{1,2,3}

¹*Earth System Modelling, School of Engineering & Design, Technical University of Munich, Germany*

²*Potsdam Institute for Climate Impact Research, Telegraphenberg A31, Potsdam, 14473, Germany*

³*Department of Mathematics and Global Systems Institute, University of Exeter, UK*

Given the likely bistability of the Atlantic Meridional Overturning Circulation (AMOC) and its recently inferred weakening, it is important to investigate the capability of identifying robust precursor signals for a possible future AMOC collapse. Dansgaard-Oeschger (DO) events, manifested most clearly as abrupt Northern-Atlantic temperature jumps during glacial conditions, likely reflect past switches between strong and weak AMOC modes. Previous studies find statistical precursor signals for the DO warming transitions associated with a strengthening AMOC. Statistical precursor signals for the abrupt DO cooling transitions, presumably associated with AMOC transitions from the strong to the weak mode, have not been identified although these would be practically much more relevant given the concern of a future AMOC collapse. Here we identify robust and statistically significant precursor signals for several DO cooling transitions from Greenland ice core records, using the concept of critical slowing down. The main source of predictability stems from so-called rebound event, humps in the temperature observed at the end of interstadial, some decades to

21 **centuries prior to the transition. Based on conceptual models, we propose several dynamical**
22 **mechanisms producing such rebound events.**

23 **Significance Statement.** Given the likely bistability of the Atlantic Meridional Overturning Cir-
24 culation (AMOC) and its recently inferred weakening, it is crucial to investigate the capability of
25 identifying precursor signals for a collapse of this key Atlantic ocean circulation system. In this
26 study we find statistical precursor signals for past abrupt northern Atlantic cooling events that are
27 supposedly associated with AMOC transitions to its weak state. We provide a theory that bridges
28 the gap between observing statistical precursor signals and the precursor signs empirically known
29 in paleoclimate research. Our results increase our confidence about the predictability of arguably
30 the most relevant climate tipping point and provide new insights regarding tipping points in the
31 climate system.

32 **Introduction**

33 A tipping point is a threshold in a forcing or control parameter, at which a small additional pertur-
34 bation causes a qualitative change in the state of the system under consideration^[1]. Once a tipping
35 point is passed, a system can transition abruptly to an alternative stable or oscillatory state^[2]. The
36 existence of climate tipping points and the possibility of abrupt transitions had been theoretically
37 predicted since the early 1960s^[2,3]. Paleoclimate evidence supports that abrupt climate changes due
38 to crossing tipping points actually occurred in the past^[2,4-6]. Recent observational and modelling
39 evidence suggest the existence of climate tipping elements in the present Earth, which pose ar-
40 guably one of the greatest risks in the context of anthropogenic global warming^[1,2]. The Atlantic

41 Meridional Overturning Circulation (AMOC) is considered the most important global-scale tip-
42 ping element^[1,2,6]. Recent studies have inferred that the AMOC is currently at its weakest in at least
43 a millennium^[7,8]; projections of the AMOC strength in the next hundred years are model-dependent,
44 but the declining AMOC trend is projected to continue in the coming century^[9].

45 The theory of critical slowing down (CSD) provides a framework to anticipate bifurcation-
46 induced transitions^[2,10-16]. The framework is based on the fact that the stability of a stable state
47 is gradually lost as the system approaches the bifurcation point. Theoretically, the variance of
48 the fluctuations around the fixed point diverges and the autocorrelation with a sufficiently small
49 lag increases toward 1 at the critical point of a codimension-one bifurcation (Methods)^[2,11,16]. Nu-
50 merical studies show that these statistical precursor signals (SPS) can anticipate simulated AMOC
51 collapses^[17,18]. Moreover, based on further refined CSD indicators, evidence of stability loss in the
52 North Atlantic in the course of the last century have been inferred from sea-surface temperature
53 and salinity data, which might indicate that the observed AMOC weakening is indeed associated
54 with a loss of stability^[14]. To put these signals into context we investigate here if similar SPS can
55 be detected also for past instances of AMOC collapse.

56 Dansgaard-Oeschger (DO) events are millennial-scale abrupt climate transitions during glacial
57 intervals^[19]. They are most clearly imprinted in the $\delta^{18}\text{O}$ and calcium ion concentration $[\text{Ca}^{2+}]$
58 records from the Greenland ice cores (Fig. 1)^[20,21]. The $\delta^{18}\text{O}$ and $[\text{Ca}^{2+}]$ are interpreted as prox-
59 ies for site temperature and atmospheric circulation changes, respectively. DO warmings occur
60 typically within a few decades and are followed by gradual cooling during relatively warm glacial

61 states termed interstadials, before a rapid return back to cold states referred to as stadials. The
62 amplitude of the abrupt warming transitions ranges from 5 to 16.5°C (cf. ref. ²² and references
63 therein). While the detailed mechanism of DO events remains debated²³⁻²⁷, recent studies with
64 general circulation models suggest that DO oscillations can spontaneously arise from complex
65 interactions between the AMOC, ocean stratification, atmosphere and sea ice²⁸⁻³³.

66 The DO events are considered the archetype of climate tipping behavior^{24,6}. Early works
67 found an SPS based on autocorrelation for one specific DO warming, the onset of Bølling–Allerød
68 interstadial⁵. In following works, the existence of SPS for DO warmings was questioned consid-
69 ering that DO warmings are noise-induced rather than bifurcation-induced^{34,35}. However a couple
70 of later studies^{13,36,37} detected SPS for several DO warmings either by ensemble averaging of
71 CSD indicators for many events³⁶ or by using Wavelet-transform techniques focusing on a spe-
72 cific frequency band^{13,37}. On the other hand, it has so far not been shown whether DO coolings
73 are preceded by characteristic CSD-based precursor signals as well. Given the recent AMOC
74 weakening^{7,8} and the observation-based suggestion that this weakening may be related to stability
75 loss¹⁴, it is important to investigate if CSD-based precursor signals can be detected for the DO
76 cooling transitions as well, likely associated with past AMOC collapses. In view of the concern of
77 a future AMOC collapse, such SPS of the DO coolings would in fact be practically more relevant
78 than the already discovered SPS for the DO warmings.

79 In this study we explore CSD-based precursor signals for DO cooling transitions recorded in
80 $\delta^{18}\text{O}$ and $\log_{10}[\text{Ca}^{2+}]$ ^{20,21} from three Greenland Ice Cores: NGRIP, GRIP and GISP2 (see Fig. 1 for

81 NGRIP). Multiple records are used for a robust assessment because each has regional fluctuations
82 as well as proxy- and ice-core-dependent uncertainties. The six records have been synchronized
83 and are given at 20-yr resolution^{20,21}. They continuously span the last 104 kyr b2k (kiloyears
84 before 2000 CE), beyond which only NGRIP $\delta^{18}\text{O}$ is available up to a part of Eemian interglacial.
85 In addition, we use a version of the NGRIP $\delta^{18}\text{O}$ and dust records at 5-cm depth resolution^{38,40}
86 in order to check the dependence of results on temporal resolutions, with the caveat that these
87 high-resolution records span only the last 60 kyr.

88 We follow the classification of interstadials and stadials and associated timings of DO warm-
89 ing and cooling transitions by Rasmussen et al. (2014)²⁰, where Greenland interstadials (stadials)
90 are labelled with ‘GI’ (‘GS’) with few exceptions below. A *rebound event* is a relatively abrupt
91 warming often observed before an interstadial abruptly ends⁴¹ (arrows in Figs. 1, 2 and 3). Gener-
92 ally a long rebound event accompanies a long interstadial ($R^2 = 0.95$,⁴¹). in Ref.^{20,41}, GI-14 and
93 subsequent GI-13 are seen as one long interstadial with GI-13 considered to be a strongly expressed
94 rebound event ending GI-14 because the changes in $\delta^{18}\text{O}$ and $\log_{10}[\text{Ca}^{2+}]$ during the quasi-stadial
95 GS-14 do not reach the base-line levels of adjacent stadials. Similarly GI-23.1 and GI-22 are also
96 seen as one long interstadial, and GI-22 is regarded as a rebound event (and GS-23.1 as quasi-
97 stadial)^{20,41}. Here we consider nine rebound-type events (Methods) including seven previously
98 identified rebound events^{20,41}. The start and end of each interstadial are identified at 20-yr reso-
99 lution based on both $\delta^{18}\text{O}$ and $[\text{Ca}^{2+}]$ in Ref.²⁰, where the uncertainties associated with the event
100 timings are also estimated.

101 **Results**

102 * Characteristic precursor signals of DO coolings As CSD-based indicators we consider the vari-
103 ance and lag-1 autocorrelation, calculated in rolling windows across each interstadial (see Meth-
104 ods). Since this requires a minimum length of data points, we focus on interstadials longer than
105 1000 yr after removing 2σ uncertainty ranges of the transition timings (Fig. 1, gray shades). The
106 removal of the 2σ uncertainty ranges of event timings (40 to 400 years) effectively excludes parts
107 of the transitions themselves from the calculation of the CSD indicators. The resulting 12 intersta-
108 dials (>1000 yr) of the NGRIP $\delta^{18}\text{O}$ record are magnified in Figs. 2 and 3 (top rows, blue). See SI
109 Appendix, Figs. S1–S10 for the other records.

110 For each interstadial, the nonlinear trend is estimated with a local regression method, specif-
111 ically the locally weighted scatterplot smoothing^{42,43} (Figs. 2 and 3, top row, red). In this case
112 the smoothing span α that defines the fraction of data points involved in the local regression is set
113 to 50% of each segment length. Gaussian kernel smoothing gives similar results. The difference
114 between the record and the nonlinear trend gives the approximately stationary residual fluctuations
115 (second row). The CSD indicators are calculated from the residual series over a rolling window.
116 In Figs. 2 and 3 the rolling window size W is set to 50% of each segment length (a default value in
117 Ref.⁵). The smoothing span α and the rolling window size W are taken as fractions of individual
118 interstadial length because time scales of local fluctuations (such as the duration of rebound events)
119 change with the entire duration of interstadial. We examine the dependence of the results on α and
120 W as part of our robustness tests.

121 The variance is plotted in the third row of Figs. 2 and 3. Positive trends in the variance are
122 observed for 9 out of 12 interstadials; the individual trends are statistically significant in 6 out of 12
123 cases ($p < 0.05$), based on a null model assuming the same overall variance and autocorrelation,
124 constructed by producing surrogates with randomized Fourier phases (See Methods). The lag-
125 1 autocorrelation is also plotted for the same data in the bottom row. Positive trends in lag-1
126 autocorrelation are observed for 10 out of 12 interstadials, but are statistically significant only in
127 2 cases ($p < 0.05$). In several cases (GI-24.2, 21.1, 16.1, 14-13 and 12), the lag-1 autocorrelation
128 first decreases and then increases. The drastic increases in both indicators near the end of the
129 interstadials reflect the rebound events (arrows in Figs. 2 and 3). We obtain similar results for the
130 other ice core records (SI Appendix, Figs. S1–S10). While we observe a number of positive trends
131 for all the records, the number of detected statistically significant trends depends on the record and
132 CSD indicator (SI Appendix, Table S1).

133 We check robustness of our results against changing smoothing span α and rolling window
134 size W ⁴³. We calculate the p -value for the trend of each indicator changing the smoothing span
135 between 20–70% of interstadial length (in steps of 10%) and the rolling window size between 20–
136 60% (also in 10% steps), respectively. This yields a 6×5 matrix for the p -values: Example results,
137 for GI-25 and $\delta^{18}\text{O}$, are shown in Figs. 4a (variance) and 4b (lag-1 autocorrelation). The cross
138 mark (x) indicates significant positive trends ($p < 0.05$) and the small open circle (o) indicates
139 positive trend that are significant at 10% confidence but not at 5% confidence. Full results for the
140 12 interstadials, 6 records, and two CSD indicators are shown in SI Appendix, Figs. S11–S22. We
141 consider positive trends in CSD indicators, i.e. the SPS of the transition, to be overall robust if we

142 obtain significant positive trends ($p < 0.05$) for at least half (≥ 15) of the 30 parameter sets.

143 The robustness analysis is performed for all the long interstadials of the 6 records and the
144 two CSD indicators (Fig. 4d). Among the 12 interstadials, we find at least one robust SPS for 9
145 interstadials (GI-25, 23.1, 21.1, 20, 19.2, 16, 14, 12 and 8) and multiple robust SPS for 6 (GI-25,
146 23.1, 21.1, 14, 12 and 8). If the data series is a stationary stochastic process, the probability of
147 observing a robust SPS is estimated to be 5% (Methods). Thus the observation of robust SPS for
148 36 cases (31%) over the 116 combinations of data and indicators in Fig. 4d is very unlikely to occur
149 by chance. Robust SPS are more likely to be observed in longer interstadials than in shorter ones
150 (compare Figs. 4c and 4d).

151 * Further sensitivity analyses We examine how much the rebound events affect the detection of
152 CSD-based SPS. For this purpose CSD indicators are again calculated excluding the rebound
153 events and their preceding cold spells (Methods). Only four interstadials (GI-23.1, 14, 12 and
154 8) exhibit robust SPS without the rebound events, while 8 interstadials (GI-25, 23.1, 21.1, 20, 16,
155 14, 12 and 8) exhibit robust SPS with the rebound events included (SI Appendix, Fig. 23). The
156 rebound events should hence be considered important, sometimes indispensable, sources for SPS
157 of DO coolings.

158 We also examine the dependence of the results on the time resolution of the data. Here we
159 use a high-resolution (5-cm depth) $\delta^{18}\text{O}$ record^{38,39} and a dust record⁴⁰ from the NGRIP over the
160 last 60 kyr. Since the data in these records are non-uniform in time, they are linearly resampled
161 every 5 yr before calculating CSD indicators. We focus on 11 interstadials longer than 300 yr

162 in order to have enough data points. For the dust record, three interstadials (GI-15, 8 and 7) are
163 excluded from the analysis because the original data has long parts of missing values. The CSD
164 indicators, calculated with a smoothing span of $\alpha = 50\%$ and rolling windows with $W = 50\%$, are
165 shown in SI Appendix, Figs. S24–S27. Through the robustness analyses with respect to α and W ,
166 we find at least one robust SPS for 3 out of 11 interstadials (SI Appendix, Fig. S28). The robust
167 SPS for GI-14-13 and GI-12 from the high-resolution records are consistent with those from the
168 20-yr resolution records. Moreover for GI-1, the high-resolution $\delta^{18}\text{O}$ record exhibits a robust SPS
169 in terms of lag-1 autocorrelation, although the 20-yr resolution record does not. Again, shorter
170 interstadials ($\lesssim 1000$ yr) do not show robust SPS.

171 **Discussion**

172 We detected robust precursor signals of DO cooling transitions for more than half of the long
173 (> 1000 yr) interstadials, but not for shorter interstadials. The results suggest that long intersta-
174 dials, the existence of rebound events, and the presence of precursor signals for the DO cooling
175 transitions at the end of interstadials are related (except for GI-19.2, which has no noticeable re-
176 bound event). These aspects may be related to generic properties of nonlinear dynamical systems.
177 On the basis of conceptual mathematical models (Methods), we propose four possible dynamical
178 mechanisms leading to the precursor signals of DO cooling transitions. In three out of four mech-
179 anisms, oscillations like the rebound events can systematically arise prior to the abrupt cooling
180 transitions. These modelling results justify the inclusion of the rebound events in the search for
181 precursor signals presented above.

182 1. The fold bifurcation mechanism. Since the pioneering work by Stommel³, the AMOC is
 183 considered to exhibit bistability^{4,44}. The bistability of the AMOC strength x may be conceptually
 184 modelled by a double-fold bifurcation model: $\dot{x} = f(x) + p + \xi(t)$, where $f(x)$ has two fold points
 185 like $x - x^3$ and $|x|(1 - x)$. Here we take the quadratic from $f(x) = |x|(1 - x)$, but the following
 186 arguments are qualitatively the same for $x - x^3$. The parameter p represents the surface salinity
 187 flux (i.e. negative freshwater flux), and $\xi(t)$ denotes white Gaussian noise. The unperturbed model
 188 for $\xi(t) = 0$ has equilibria on an S-shaped curve: $f(x) + p = 0$ (Fig. 5a, green). The state $x(t)$
 189 initially on the upper stable branch jumps down to the lower stable branch as p decreases across the
 190 fold bifurcation point at $p = -0.25$. The variance and the autocorrelation of the local fluctuations
 191 (i.e. the CSD indicators) increase as p approaches the fold bifurcation point^{2,11}.

192 2. Stochastic slow-fast oscillation mechanism. The FitzHugh-Nagumo (FHN) system is a
 193 prototypical model for slow-fast oscillations and excitability⁴⁵. It is often invoked for conceptual
 194 models of DO oscillations^{29,46-49}. An FHN-type model of DO oscillations is obtained by intro-
 195 ducing a slow variable y into the fold bifurcation model: $\dot{x} = \frac{1}{\tau_x}(|x|(1 - x) + y + p) + \xi(t)$,
 196 $\dot{y} = \frac{1}{\tau_y}(-x - y)$, where τ_x and τ_y are time-scale parameters ($\tau_x \ll \tau_y$). Invoking the salt-oscillator
 197 hypothesis for DO oscillations suggested by the comprehensive climate model simulations that
 198 are successful in reproducing DO cycles⁵⁰, we may interpret y as the salinity in the polar halo-
 199 cline surface mixed layer, which gradually decreases (increases) when the AMOC intensity x is
 200 strong (weak). Here we consider the case that the unperturbed system is excitable. For example for
 201 $p = 0.26$, the unperturbed system has a stable equilibrium near the upper fold point of the S-shaped
 202 critical manifold, $\{(x, y) \in \mathbb{R}^2 \mid y = -|x|(1 - x) - p\}$ (Fig. 5c, green), but stochastic oscillations

203 sustain under the dynamical noise forcing $\xi(t)$ (Figs. 5b and 5c, blue). Due to the time-scale separation
204 ($\tau_x \ll \tau_y$), the oscillations occur along the attracting parts of the critical manifold (Fig. 5c).
205 Because y is much slower than x , the dynamics of x is similar to the dynamics of the fold bifurca-
206 tion model with slowly changing y . Consequently SPS can be observed near the fold point of the
207 critical manifold (SI Appendix, Fig. S29). The increase of the variance prior to the transitions in
208 the FHN model is reported also in Ref.⁵¹. Since the unperturbed system has an equilibrium near the
209 upper fold point, the motion is stagnant near the fold point. This provides favorable conditions for
210 observing SPS. The state jumps from the upper branch of the critical manifold to its lower branch
211 often after an upward jump induced by noise. These upward jumps resemble the rebound events
212 prior to DO coolings. The overall phenomenon is the same in the self-sustained oscillation regime
213 of the FHN model as long as the equilibrium locates near the fold point of the critical manifold.

214 3. Hopf bifurcation mechanism. In contrast to the fold bifurcation, the Hopf bifurcation
215 manifests oscillatory instability⁵². In several ocean box models, the thermohaline circulation is
216 destabilized via a Hopf bifurcation rather than a fold bifurcation⁵³⁻⁵⁵. It is also considered a po-
217 tential generating mechanism of DO oscillations in a low-order coupled climate model⁵⁶ and in a
218 comprehensive climate model²⁸. Assume that the parameter p decreases slowly in the FHN-type
219 model (Figs. 5d and 5e). The underlying dynamics changes from the stable equilibrium to the
220 limit-cycle oscillations at the Hopf bifurcation point $p = (1 - \tau_x/\tau_y)^2/4$ (Methods). If stochastic
221 forcing is added to the system, noise-induced small oscillations can appear prior to the onset of the
222 limit-cycle oscillations (Fig. 5d and 5e). The precursor oscillations resemble rebound events, while
223 their shape depends on the noise. Again SPS can be observed near the Hopf bifurcation point (SI

224 Appendix, Fig. S30)^{[2][16][51]}.

225 4. Mixed-mode oscillation mechanism. Mixed-mode oscillations (MMOs) are periodic
226 oscillations consisting of small and large-amplitude oscillations^[57]. They often arise in systems
227 with one fast variable and two slow variables^[57]. For example, MMOs appear in the FHN-type
228 model with a slight extension: $\dot{x} = \frac{1}{\tau_x}(|x|(1-x) + y + p)$, $\dot{y} = \frac{1}{\tau_y}(-x - y + k(z - y))$
229 and $\dot{z} = \frac{1}{\tau_z}(-x - z + k(y - z))$, where z is another slow variable with time scale τ_z ($\gg \tau_x$)
230 and k is the diffusive-coupling constant between slow variables. We interpret y as the surface
231 salinity in the North Atlantic convection region that directly affects the AMOC strength x again,
232 and z as the surface salinity outside the convection region that affects the surface salinity y in
233 the convection region via mixing. For specific parameter settings (Methods), the system has
234 an unstable equilibrium $(x, y, z) = (\sqrt{p}, -\sqrt{p}, -\sqrt{p})$ of saddle-focus type, with one stable di-
235 rection with a negative real eigenvalue and a two-dimensional unstable manifold with complex
236 eigenvalues with positive real part. The slow-fast oscillations occur along the critical manifold
237 $\{(x, y, z) \in \mathbb{R}^3 \mid y = -|x|(1-x) - p\}$ (Figs. 5f and 5g). However, due to the saddle-focus equilib-
238 rium on the critical manifold, the trajectory is attracted toward the saddle from the direction of the
239 stable manifold (black segment) and repelled from it in a spiralling fashion. The striking point is
240 the systematic occurrence of small-amplitude oscillations prior to the abrupt transition, which also
241 resemble the rebound events prior to the DO cooling transitions. A more realistic time series is
242 obtained if an observation noise is added on $x(t)$ (SI Appendix, Fig. S31). Then SPS can be stably
243 observed near the fold point of the critical manifold.

244 We have proposed four possible dynamical mechanisms for the DO cooling transitions that
245 can manifest precursor signals and behavior resembling the rebound events found in the ice core
246 records: The precursor signals for the DO coolings can be (i) strict critical slowing down due to the
247 approaching of a fold bifurcation, (ii) critical slowing down in a wider sense, in stochastic slow-
248 fast oscillations, (iii) noise-induced oscillations prior to Hopf bifurcations, or (iv) the signal of
249 mixed-mode oscillations. While the details of these mechanisms are different, they are all related
250 to the fold points of the equilibrium curve or the critical manifolds. Consequently the precursor
251 signals can be detected by the conventional CSD indicators. Note that the precursor behavior like
252 the rebound events occur when the modelled interstadials have equilibria on the critical manifold
253 with marginal stability (i.e., the equilibrium has neither strong stability leading to a permanent
254 state nor strong instability leading to brief interstadials) (Figs. 5b–5g). Then the duration of the
255 modelled interstadial is comparatively long in relation to the marginal stability. This provides an
256 explanation why the rebound events in the ice core records and significant precursor signals are
257 observed only for long interstadials ($\gtrsim 1000$ yr).

258 In summary, we have provided robust evidence that the DO cooling transitions from inter-
259 stadial to stadial glacial conditions are preceded by characteristic precursor signals due to CSD.
260 These signals are robust across CSD indicators, ice core records and proxy variables. Rebound
261 events prior to the cooling transitions are important in producing the statistical precursor signals.
262 We have proposed four different dynamical mechanisms to explain the role of these rebound events
263 and more generally to understand the physical reasons for the revealed predictability of the DO
264 cooling transitions. Because these transitions are most likely associated with AMOC collapses,

265 our results provide empirical evidence from past climate records that it should indeed be possible
266 to anticipate AMOC transitions from the strong to the weak mode based on CSD indicators.

267 **Methods**

268 * **Data:** Greenland ice core records We use $\delta^{18}\text{O}$ and $\log_{10}[\text{Ca}^{2+}]$ records^{20,21} from Greenland
269 ice cores: NGRIP, GRIP and GISP2. These records have been synchronized and are published at
270 20-yr resolution. They continuously span the last 104 kyr b2k, beyond which only NGRIP $\delta^{18}\text{O}$
271 is available up to a part of Eemian interglacial. In addition to the 20-yr-resolution records, we
272 also use high-resolution (5-cm depth) $\delta^{18}\text{O}$ ^{38,39} and dust⁴⁰ records from the NGRIP over the last
273 60 kyr. We use the classification of Greenland interstadials (GI) and stadials (GS) by Rasmussen
274 et al. (2014)²⁰.

275 *A rebound event* is an abrupt warming often observed before an interstadial abruptly ends⁴¹.
276 Capron et al. (2010) describe warmings at the end of interstadials GI-11, GI-12, GI-16 and GI-21
277 as rebound events and also GI-13 and GI-22 as rebound events⁴¹. Consequently, the composition
278 of GI-14, GS-14 and GI-13 is considered one long interstadial, and also the composition of GI-
279 23.1, GS-23.1 and GI-22 is considered one long interstadial^{20,41}. GI-20a is also recognized as
280 a rebound event in Ref.²⁰. Given that the rebound events are warmings following a colder spell
281 during interstadial conditions that does not reach the stadial levels²⁰, we regard the following nine
282 epochs as rebound-type events: GI-8a, the hump at the end of GI-11 (42240–~42500 yr b2k), GI-
283 12a, GI-13, the hump at the end of GI-16.1 (56500–~56900 yr b2k), GI-20a, GI-21.1c-b-a (two

284 warming transitions), GI-22 and GI-25a. When we examine the effect of rebound events on our
285 results, we exclude the entire parts including the cold spells prior to the rebound events.

286 The start (warming) and end (cooling) of each DO event are identified in 20-yr resolution
287 based on both $\delta^{18}\text{O}$ and $[\text{Ca}^{2+}]$ in Ref.^[20]. The estimated uncertainty of event timing varies event
288 by event. We remove the 2σ uncertainty range of the event timing (40 to 400 years) estimated in
289 Ref.^[20] from our calculation of CSD indicators.

290 * Statistical indicators of critical slowing down Based on the theory of critical slowing down
291 (CSD), we posit that the stability of a dynamical system perturbed by noise is gradually lost as
292 the system approaches a bifurcation point^{[2][11][16]}. For the fold bifurcation, the variance of the fluc-
293 tuations around a local stable state diverges and the autocorrelation function of the fluctuations
294 increases toward 1 at any lag τ . The same is true for the transcritical as well as the pitchfork
295 bifurcation^{[2][16]}. For the Hopf bifurcation, the variance increases, but the autocorrelation function
296 of the form $C(\tau) = e^{\mu|\tau| \cos \omega\tau}$ may increases or decreases depending on τ , where μ and $\pm\omega i$ are the
297 real and imaginary parts of the complex eigenvalues of the Jacobian matrix of the local linearized
298 system^{[2][16]}. Nevertheless the autocorrelation function $C(\tau)$ increases for sufficiently small τ . These
299 characteristics can be used to anticipate abrupt transitions cause by codimension-one bifurcations.
300 For time discrete series, we follow previous studies and calculate lag-1 autocorrelation.

301 Prior to calculating CSD indicators, we estimate the local stable state by using a local re-
302 gression method called the locally weighted scatterplot smoothing (LOESS)^{[42][43]}. The polynomial
303 degree is set to 1, i.e., the smoothing is performed with the local linear fit. The smoothing span

304 parameter α that defines the fraction of data points involved in the local regression is set to 50% of
305 each segment length in Figs. 2 and 3. However, we examine the dependence of results on α over
306 the range 20–70%. The difference between the record and the smoothed one gives the residual
307 fluctuations. The CSD indicators, i.e., variance and lag-1 autocorrelation, are calculated for the
308 residuals over a rolling window. The size of this rolling window is set to 50% of the record in
309 Figs. 2 and 3, but it is changed over the range 20–60% to test robustness.

310 * Probability of observing robust precursor signals The statistical significance of precursor signals
311 of critical transitions, in terms of positive trends of CSD indicators, is assessed by hypothesis
312 testing^[13,37,43,58]. We consider as null model a stationary stochastic process with preserved variance
313 and autocorrelation. The n surrogate data are prepared from the original residual data series by
314 the phase-randomization method, thus preserving the variance and autocorrelation function of the
315 original time series via Wiener-Khinchin theorem. Here we take $n = 1000$. The linear trend
316 (a_0) of the CSD indicator for the original residual time series and the linear trends (a_s) of CSD
317 indicators for the surrogate data are calculated. We consider the precursor signal of the original
318 series statistically significant if the probability of $a_s > a_o$ (p -value) is less than 0.05. Thus, if
319 the original data is already a stationary stochastic process (exhibiting no CSD), one should expect
320 spuriously significant results at a probability of 0.05 by definition. In principle this is independent
321 of the smoothing span α as well as the rolling window size W used for calculating CSD indicators.
322 We consider a precursor signal robust if we find at least 15 significant cases ($p < 0.05$) for 30
323 combinations of α and W . Then the probability of observing a robust precursor signal can be
324 shown to be 0.05. In order to check this numerically, we generate 5000 surrogates of the original

325 $\delta^{18}\text{O}$ series of interstadial GI-25 and calculate the probability of finding robust precursor signals.
326 The resulting fractions are 0.044 for the variance and 0.042 for the lag-1 autocorrelation, which
327 are close to 0.05. For the case of GI-12, we obtain 0.042 for the variance and 0.052 for the lag-1
328 autocorrelation, again close to 0.05. These results support that the probability of observing a robust
329 precursor signal is 5% if the data are stationary stochastic processes.

330 * Candidate mechanisms for DO cooling transitions Here we describe specific settings for four
331 conceptual models representing different candidate mechanisms for the DO cooling transitions.
332 Stochastic differential equations below are solved with the Euler-Maruyama method with step size
333 of 10^{-3} .

334 1. The bistability of the AMOC strength x can be conceptually modelled by a double-fold
335 bifurcation model: $\dot{x} = f(x) + p + \xi(t)$, where $f(x)$ has two fold points. Here for f one can use
336 either $f(x) = x - x^3$ or $f(x) = |x|(1 - x)$. We take the quadratic function $f(x) = |x|(1 - x)$
337 that arises in the original Stommel model^{31,41,44}. The parameter p represents the surface salinity
338 flux (i.e., negative freshwater flux). $\xi(t)$ is white Gaussian noise, e.g. freshwater perturbations or
339 weather forcing. In Fig. 5a, the initial condition is taken at $x(0) = 1.1$, near the upper stable fixed
340 point of the unperturbed system. The parameter p is then slowly decreased from 0.1 to -0.4 over
341 the period from $t = 0$ to 500, to trigger the bifurcation-induced transition.

342 2. The FitzHugh-Nagumo-type (FHN-type) system is a prototypical model of slow-fast os-
343 cillators and often invoked for conceptual models of DO oscillations^{29,46-49}. The FHN-type model
344 subjected to dynamical noise is obtained by introducing a slow variable y into the fold bifurcation

345 model: $\dot{x} = \frac{1}{\tau_x}(|x|(1-x) + y + p) + \xi(t)$, $\dot{y} = \frac{1}{\tau_y}(-x - y)$, where τ_x and τ_y are time-scale param-
346 eters ($\tau_x \ll \tau_y$). Following the salt-oscillator hypothesis to explain DO cycles⁵⁰, we may interpret
347 y as the salinity in the polar halocline surface mixed layer, which decreases (increases) when the
348 AMOC is strong (weak). In turn, the decreased (increased) surface salinity y inhibits (promotes)
349 convective activity and weakens (strengthens) the AMOC x . In the case of Figs. 5b and 5c we set
350 $p = 0.26$, $\tau_x = 0.01$, $\tau_y = 1$ and $\langle \xi^2 \rangle = 0.3$. The x -nullcline (critical manifold) of the unperturbed
351 system is $y = -|x|(1-x) - p$ (Fig. 5c, green) and the y -nullcline is the $y = -x$ (Fig. 5c, magenta
352 dashed). The intersection of the x - and y -nullclines is the equilibrium point of the unperturbed
353 system $(\sqrt{p}, -\sqrt{p})$, which is near the fold point of the critical manifold in this parameter setting.

354 3. For demonstrating the Hopf bifurcation mechanism in Figs. 5d and 5e, the same stochastic
355 FHN-type model is used with $\tau_x = 0.01$, $\tau_y = 1$ and $\langle \xi^2 \rangle = 0.05$, but here p is gradually decreased
356 from 0.3 to 0.2, over a period of 10 time units. For $0.2 < p < 0.3$, the underlying deterministic
357 system has a unique equilibrium point at $(x, y) = (\sqrt{p}, -\sqrt{p})$. The Hopf bifurcation of the equilib-
358 rium occurs if the complex eigenvalues of the Jacobian matrix at the equilibrium passes the imagi-
359 nary axis⁵². In the present case, the eigenvalues are $\lambda_{\pm} = \frac{1}{2} \left\{ \frac{1-2\sqrt{p}}{\tau_x} - \frac{1}{\tau_y} \pm \sqrt{\left(\frac{1-2\sqrt{p}}{\tau_x} - \frac{1}{\tau_y}\right)^2 - \frac{8\sqrt{p}}{\tau_x\tau_y}} \right\}$,
360 which are complex for $\frac{1}{4}\left(1 + \frac{\tau_x}{\tau_y} - 2\sqrt{\frac{\tau_x}{\tau_y}}\right)^2 < p < \frac{1}{4}\left(1 + \frac{\tau_x}{\tau_y} + 2\sqrt{\frac{\tau_x}{\tau_y}}\right)^2$. In this range of p , the real
361 part of λ_{\pm} changes from negative to positive at the Hopf bifurcation point: $p_H = (1 - \tau_x/\tau_y)^2/4$.
362 For $\tau_x/\tau_y = 0.01$, $p_H = 0.245025$.

363 4. The mixed-mode oscillation model is obtained if the FHN-type model is extended to have
364 multiple interacting slow variables. E.g., $\dot{x} = \frac{1}{\tau_x}(|x|(1-x) + y + p)$, $\dot{y} = \frac{1}{\tau_y}(-x - y + k(z - y))$

365 and $\dot{z} = \frac{1}{\tau_z}(-x - z + k(y - z))$, where z is another slow variable with time scale $\tau_z (\gg \tau_x)$ and k is
366 the diffusive coupling constant between slow variables. We interpret y as the surface salinity in the
367 North Atlantic convection region, which directly affects the AMOC strength x , and z as the surface
368 salinity outside the convection region that affects the surface salinity y in the convection region via
369 mixing. We set $\tau_x = 0.02$, $\tau_y = 2$, $\tau_z = 4$, $p = 0.225$ and $k = 0.8$. This system has an unstable
370 equilibrium $(x, y, z) = (\sqrt{p}, -\sqrt{p}, -\sqrt{p})$ of saddle-focus type, with one stable direction with a
371 negative real eigenvalue -0.67 and a two-dimensional unstable manifold with complex conjugate
372 eigenvalues with positive real part $0.94 \pm 4.7i$.

373 Reference

- 374 1. Armstrong McKay, D. I. *et al.* Exceeding 1.5 c global warming could trigger multiple climate
375 tipping points. *Science* **377**, eabn7950 (2022).
- 376 2. Boers, N., Ghil, M. & Stocker, T. F. Theoretical and paleoclimatic evidence for abrupt transi-
377 tions in the earth system. *Environmental Research Letters* **17**, 093006 (2022).
- 378 3. Stommel, H. Thermohaline convection with two stable regimes of flow. *Tellus* **13**, 224–230
379 (1961).
- 380 4. Alley, R. B. *et al.* Abrupt climate change. *science* **299**, 2005–2010 (2003).
- 381 5. Dakos, V. *et al.* Slowing down as an early warning signal for abrupt climate change. *Proceed-*
382 *ings of the National Academy of Sciences* **105**, 14308–14312 (2008).
- 383

- 384 6. Brovkin, V. *et al.* Past abrupt changes, tipping points and cascading impacts in the earth
385 system. *Nature Geoscience* **14**, 550–558 (2021).
- 386 7. Rahmstorf, S. *et al.* Exceptional twentieth-century slowdown in atlantic ocean overturning
387 circulation. *Nature climate change* **5**, 475–480 (2015).
- 388 8. Caesar, L., Rahmstorf, S., Robinson, A., Feulner, G. & Saba, V. Observed fingerprint of a
389 weakening atlantic ocean overturning circulation. *Nature* **556**, 191–196 (2018).
- 390 9. Masson-Delmotte, V. *et al.* Climate change 2021: the physical science basis. *Contribution*
391 *of working group I to the sixth assessment report of the intergovernmental panel on climate*
392 *change* **2** (2021).
- 393 10. Carpenter, S. R. & Brock, W. A. Rising variance: a leading indicator of ecological transition.
394 *Ecology letters* **9**, 311–318 (2006).
- 395 11. Scheffer, M. *et al.* Early-warning signals for critical transitions. *Nature* **461**, 53–59 (2009).
- 396 12. Kuehn, C. A mathematical framework for critical transitions: normal forms, variance and
397 applications. *Journal of Nonlinear Science* **23**, 457–510 (2013).
- 398 13. Boers, N. Early-warning signals for dansgaard-oeschger events in a high-resolution ice core
399 record. *Nature communications* **9**, 2556 (2018).
- 400 14. Boers, N. Observation-based early-warning signals for a collapse of the atlantic meridional
401 overturning circulation. *Nature Climate Change* **11**, 680–688 (2021).

- 402 15. Boers, N. & Rypdal, M. Critical slowing down suggests that the western greenland ice sheet is
403 close to a tipping point. *Proceedings of the National Academy of Sciences* **118**, e2024192118
404 (2021).
- 405 16. Bury, T. M., Bauch, C. T. & Anand, M. Detecting and distinguishing tipping points using
406 spectral early warning signals. *Journal of the Royal Society Interface* **17**, 20200482 (2020).
- 407 17. Boulton, C. A., Allison, L. C. & Lenton, T. M. Early warning signals of atlantic meridional
408 overturning circulation collapse in a fully coupled climate model. *Nature communications* **5**,
409 1–9 (2014).
- 410 18. Held, H. & Kleinen, T. Detection of climate system bifurcations by degenerate fingerprinting.
411 *Geophysical Research Letters* **31** (2004).
- 412 19. Dansgaard, W. *et al.* Evidence for general instability of past climate from a 250-kyr ice-core
413 record. *Nature* **364**, 218–220 (1993).
- 414 20. Rasmussen, S. O. *et al.* A stratigraphic framework for abrupt climatic changes during the last
415 glacial period based on three synchronized greenland ice-core records: refining and extending
416 the intimate event stratigraphy. *Quaternary Science Reviews* **106**, 14–28 (2014).
- 417 21. Seierstad, I. K. *et al.* Consistently dated records from the greenland grip, gisp2 and ngrip
418 ice cores for the past 104 ka reveal regional millennial-scale $\delta^{18}O$ gradients with possible
419 heinrich event imprint. *Quaternary Science Reviews* **106**, 29–46 (2014).
- 420 22. Kindler, P. *et al.* Temperature reconstruction from 10 to 120 kyr b2k from the ngrip ice core.
421 *Climate of the Past* **10**, 887–902 (2014).

- 422 23. Broecker, W. S., Peteet, D. M. & Rind, D. Does the ocean-atmosphere system have more than
423 one stable mode of operation? *Nature* **315**, 21–26 (1985).
- 424 24. Ganopolski, A. & Rahmstorf, S. Rapid changes of glacial climate simulated in a coupled
425 climate model. *Nature* **409**, 153–158 (2001).
- 426 25. Petersen, S. V., Schrag, D. P. & Clark, P. U. A new mechanism for dansgaard-oeschger cycles.
427 *Paleoceanography* **28**, 24–30 (2013).
- 428 26. Dokken, T. M., Nisancioglu, K. H., Li, C., Battisti, D. S. & Kissel, C. Dansgaard-oeschger
429 cycles: Interactions between ocean and sea ice intrinsic to the nordic seas. *Paleoceanography*
430 **28**, 491–502 (2013).
- 431 27. Boers, N., Ghil, M. & Rousseau, D.-D. Ocean circulation, ice shelf, and sea ice interac-
432 tions explain dansgaard-oeschger cycles. *Proceedings of the National Academy of Sciences*
433 201802573 (2018).
- 434 28. Peltier, W. R. & Vettoretti, G. Dansgaard-oeschger oscillations predicted in a comprehensive
435 model of glacial climate: A “kicked” salt oscillator in the atlantic. *Geophysical Research*
436 *Letters* **41**, 7306–7313 (2014).
- 437 29. Vettoretti, G., Ditlevsen, P., Jochum, M. & Rasmussen, S. O. Atmospheric co2 control of
438 spontaneous millennial-scale ice age climate oscillations. *Nature Geoscience* **15**, 300–306
439 (2022).

- 440 30. Brown, N. & Galbraith, E. D. Hosed vs. unhosed: interruptions of the atlantic meridional over-
441 turning circulation in a global coupled model, with and without freshwater forcing. *Climate*
442 *of the Past* **12** (2016).
- 443 31. Klockmann, M., Mikolajewicz, U., Kleppin, H. & Marotzke, J. Coupling of the subpolar
444 gyre and the overturning circulation during abrupt glacial climate transitions. *Geophysical*
445 *Research Letters* **47**, e2020GL090361 (2020).
- 446 32. Zhang, X. *et al.* Direct astronomical influence on abrupt climate variability. *Nature Geoscience*
447 **14**, 819–826 (2021).
- 448 33. Kuniyoshi, Y., Abe-Ouchi, A., Sherriff-Tadano, S., Chan, W.-L. & Saito, F. Effect of cli-
449 matic precession on dansgaard-oeschger-like oscillations. *Geophysical Research Letters* **49**,
450 e2021GL095695 (2022).
- 451 34. Ditlevsen, P. D. & Johnsen, S. J. Tipping points: early warning and wishful thinking. *Geo-*
452 *physical Research Letters* **37** (2010).
- 453 35. Lenton, T., Livina, V., Dakos, V. & Scheffer, M. Climate bifurcation during the last deglacia-
454 tion? *Climate of the Past* **8**, 1127–1139 (2012).
- 455 36. Cimatoribus, A., Drijfhout, S., Livina, V. & Van Der Schrier, G. Dansgaard–oeschger events:
456 bifurcation points in the climate system. *Climate of the Past* **9**, 323–333 (2013).
- 457 37. Rypdal, M. Early-warning signals for the onsets of greenland interstadials and the younger
458 dryas–preboreal transition. *Journal of Climate* **29**, 4047–4056 (2016).

- 459 38. members, N. G. I. C. P. *et al.* High resolution record of northern hemisphere climate extending
460 into the last interglacial period. *Nature* **431**, 147–151 (2004).
- 461 39. Gkinis, V., Simonsen, S. B., Buchardt, S. L., White, J. & Vinther, B. M. Water isotope diffusion
462 rates from the northgrip ice core for the last 16,000 years—glaciological and paleoclimatic
463 implications. *Earth and Planetary Science Letters* **405**, 132–141 (2014).
- 464 40. Ruth, U., Wagenbach, D., Steffensen, J. P. & Bigler, M. Continuous record of microparticle
465 concentration and size distribution in the central greenland ngrip ice core during the last glacial
466 period. *Journal of Geophysical Research: Atmospheres* **108** (2003).
- 467 41. Capron, E. *et al.* Millennial and sub-millennial scale climatic variations recorded in polar ice
468 cores over the last glacial period. *Climate of the Past* **6**, 345–365 (2010).
- 469 42. Cleveland, W., Grosse, E. & Shyu, W. Local regression models. chapter 8 in statistical models
470 in s (jm chambers and tj hastie eds.), 608 p. *Wadsworth & Brooks/Cole, Pacific Grove, CA*
471 (1992).
- 472 43. Dakos, V. *et al.* Methods for detecting early warnings of critical transitions in time series
473 illustrated using simulated ecological data. *PloS one* **7**, e41010 (2012).
- 474 44. Rahmstorf, S. Ocean circulation and climate during the past 120,000 years. *Nature* **419**,
475 207–214 (2002).
- 476 45. FitzHugh, R. Impulses and physiological states in theoretical models of nerve membrane.
477 *Biophysical journal* **1**, 445 (1961).

- 478 46. Roberts, A. & Saha, R. Relaxation oscillations in an idealized ocean circulation model. *Climate dynamics* **48**, 2123–2134 (2017).
479
- 480 47. Mitsui, T. & Crucifix, M. Influence of external forcings on abrupt millennial-scale climate
481 changes: a statistical modelling study. *Climate Dynamics* **48**, 2729–2749 (2017).
- 482 48. Lohmann, J. & Ditlevsen, P. D. A consistent statistical model selection for abrupt glacial
483 climate changes. *Climate dynamics* **52**, 6411–6426 (2019).
- 484 49. Riechers, K., Mitsui, T., Boers, N. & Ghil, M. Orbital insolation variations, intrinsic climate
485 variability, and quaternary glaciations. *Climate of the Past* **18**, 863–893 (2022).
- 486 50. Vettoretti, G. & Peltier, W. R. Fast physics and slow physics in the nonlinear dansgaard–
487 oeschger relaxation oscillation. *Journal of Climate* **31**, 3423–3449 (2018).
- 488 51. Meisel, C. & Kuehn, C. Scaling effects and spatio-temporal multilevel dynamics in epileptic
489 seizures. *PLoS One* **7**, e30371 (2012).
- 490 52. Strogatz, S. H. *Nonlinear dynamics and chaos: with applications to physics, biology, chem-*
491 *istry, and engineering* (CRC Press, 2018).
- 492 53. Alkhayuon, H., Ashwin, P., Jackson, L. C., Quinn, C. & Wood, R. A. Basin bifurcations, os-
493 cillatory instability and rate-induced thresholds for atlantic meridional overturning circulation
494 in a global oceanic box model. *Proceedings of the Royal Society A* **475**, 20190051 (2019).
- 495 54. Abshagen, J. & Timmermann, A. An organizing center for thermohaline excitability. *Journal*
496 *of physical oceanography* **34**, 2756–2760 (2004).

- 497 55. Sakai, K. & Peltier, W. R. A dynamical systems model of the dansgaard-oeschger oscillation
498 and the origin of the bond cycle. *Journal of climate* **12**, 2238–2255 (1999).
- 499 56. Timmermann, A., Gildor, H., Schulz, M. & Tziperman, E. Coherent resonant millennial-scale
500 climate oscillations triggered by massive meltwater pulses. *Journal of Climate* **16**, 2569–2585
501 (2003).
- 502 57. Desroches, M. *et al.* Mixed-mode oscillations with multiple time scales. *Siam Review* **54**,
503 211–288 (2012).
- 504 58. Theiler, J., Eubank, S., Longtin, A., Galdrikian, B. & Farmer, J. D. Testing for nonlinearity
505 in time series: the method of surrogate data. *Physica D: Nonlinear Phenomena* **58**, 77–94
506 (1992).

507 **Author contributions statement** T.M. conceived the study and conducted the analyses with contributions
508 from N.B. Both authors discussed and interpreted results. T.M. wrote the manuscript with contributions from
509 N.B.

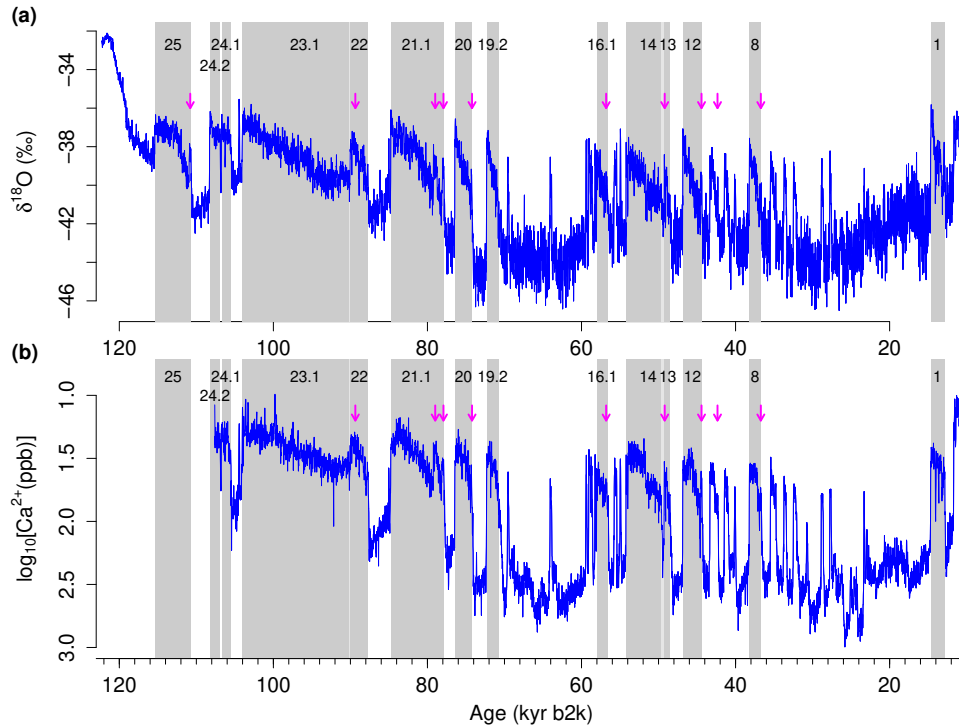
510 **Acknowledgements** The authors thank K. Riechers and M. Ben-Yami for their helpful comments. The
511 authors acknowledge funding by the Volkswagen Foundation. This is TiPES contribution #X; The TiPES
512 (“Tipping Points in the Earth System”) project has received funding from the European Union’s Horizon
513 2020 research and innovation programme under grant agreement No 820970. N.B. acknowledges fur-
514 ther funding by the European Union’s Horizon 2020 research and innovation programme under the Marie
515 Sklodowska-Curie grant agreement No. 956170, as well as from the Federal Ministry of Education and
516 Research under grant No. 01LS2001A.

517 **Competing Interests** The authors declare that they have no competing financial interests.

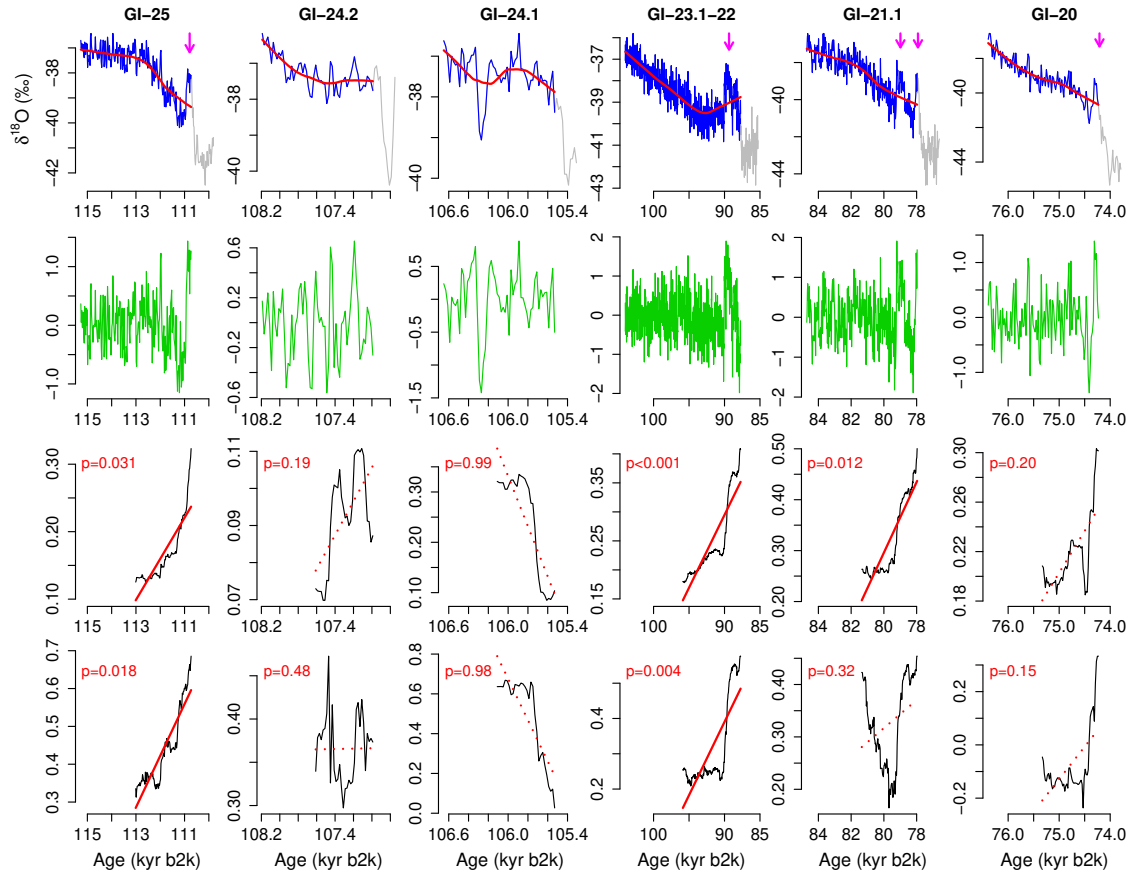
518 **Correspondence** Correspondence and requests for materials should be addressed to Takahito Mitsui (email:
519 takahito321@gmail.com).

520 **Supplementary Information (SI) Appendix** [https://github.com/takahito321/Predictability-of-DO-cooling/
521 blob/main/EWS_DO_cooling_arXiv_SI.pdf](https://github.com/takahito321/Predictability-of-DO-cooling/blob/main/EWS_DO_cooling_arXiv_SI.pdf)

522 **Figures**



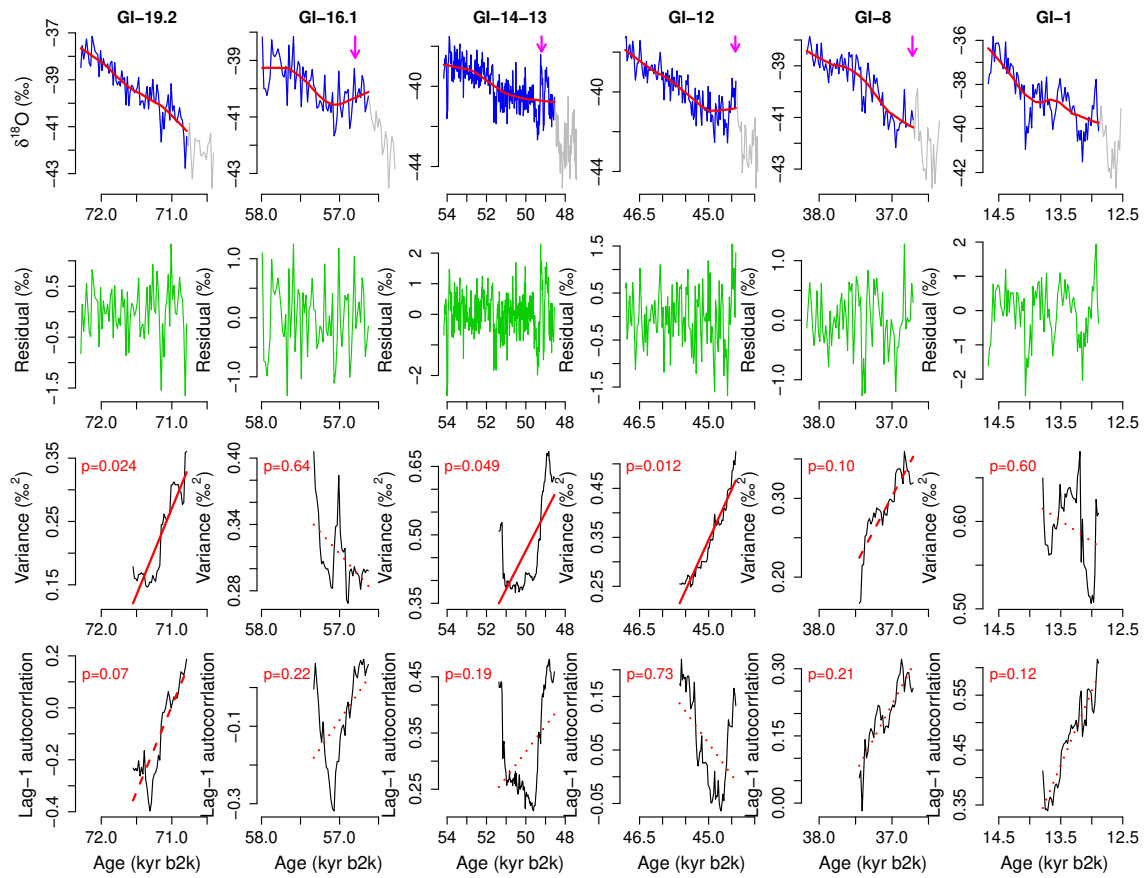
523 **Figure 1.** Greenland records from the NGRIP ice core: (a) $\delta^{18}\text{O}$ and (b) $\log_{10}[\text{Ca}^{2+}]$ ^[20,21]. The
 524 interstadial parts longer than 1000-yr are highlighted with grey shades; their numbering is given
 525 at the top of each record^[20]. The rebound events are indicated by arrows (see Methods for their
 526 list). Both records are presented at 20-yr resolution. The $\log_{10}[\text{Ca}^{2+}]$ record is available only up to
 527 DO-24.1. The compositions of GI-23.1 and GI-22, as well as of GI-14 and GI-13, are considered
 528 individual long interstadials^[20,41]. The vertical axis for $\log_{10}[\text{Ca}^{2+}]$ in (b) is reversed to ease visual
 529 comparison with the $\delta^{18}\text{O}$ record.



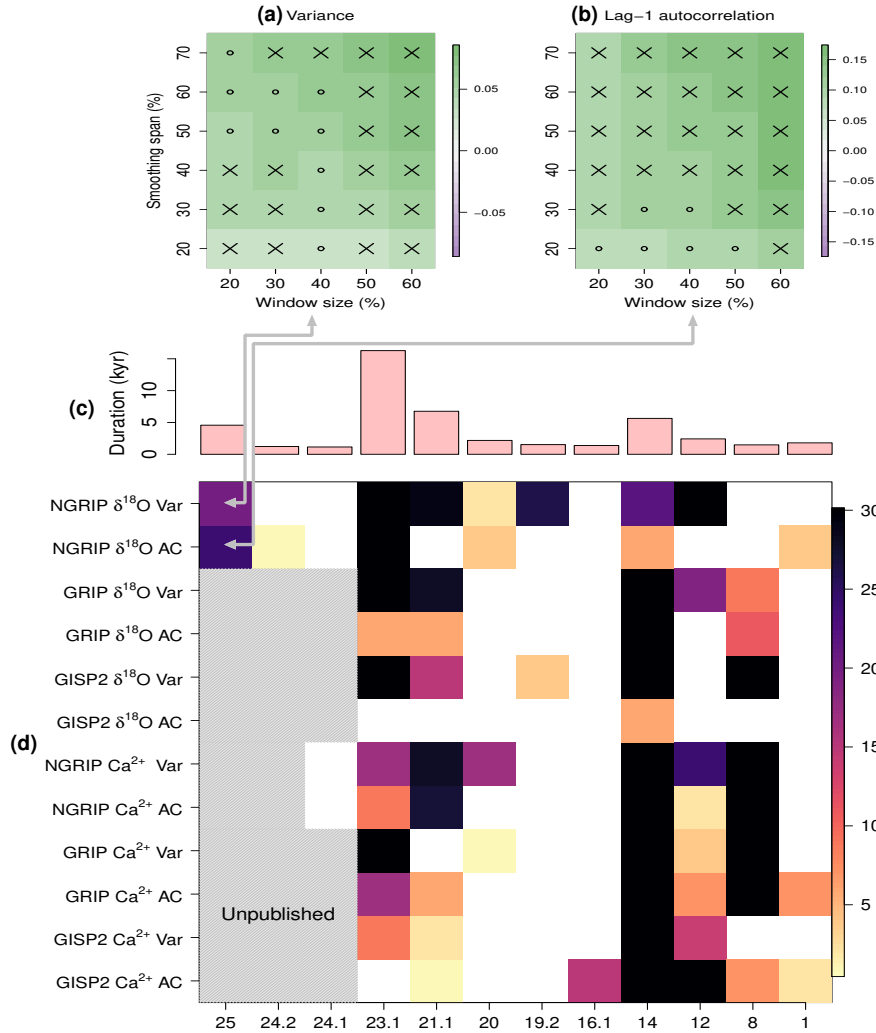
530 **Figure 2.** Analysis of CSD-based precursor signals of abrupt DO cooling transitions, for the first 6
 531 interstadials of NGRIP $\delta^{18}\text{O}$, from 115 ka to 74 kyr b2k. (Top row) Interstadials longer than 1000 yr
 532 (blue). The cooling transition and stadial parts are shown in grey^[20]. Nonlinear trends are calculated
 533 with the Locally Weighted Scatterplot Smoothing (LOESS) (red). The smoothing span α that
 534 defines the fraction of data points involved in the local regression is set to 50% of each segment
 535 length. The rebound events are indicated by arrows (Methods). (Second row) Residuals (green)
 536 resulting from subtracting the nonlinear trends (red) from the records (blue). (Third row) Variance
 537 estimate in rolling windows (black) with size equal to 50% of each segment length. Values are
 538 plotted at the right edge of each rolling window. The linear trend is shown by a solid red line for

539 $p < 0.05$, by a dashed red line for $0.05 < p < 0.1$, and by a dotted line for $p > 0.1$. (Fourth row)

540 Same as third row but for the lag-1 autocorrelation (i.e., a lag of 20 yr).

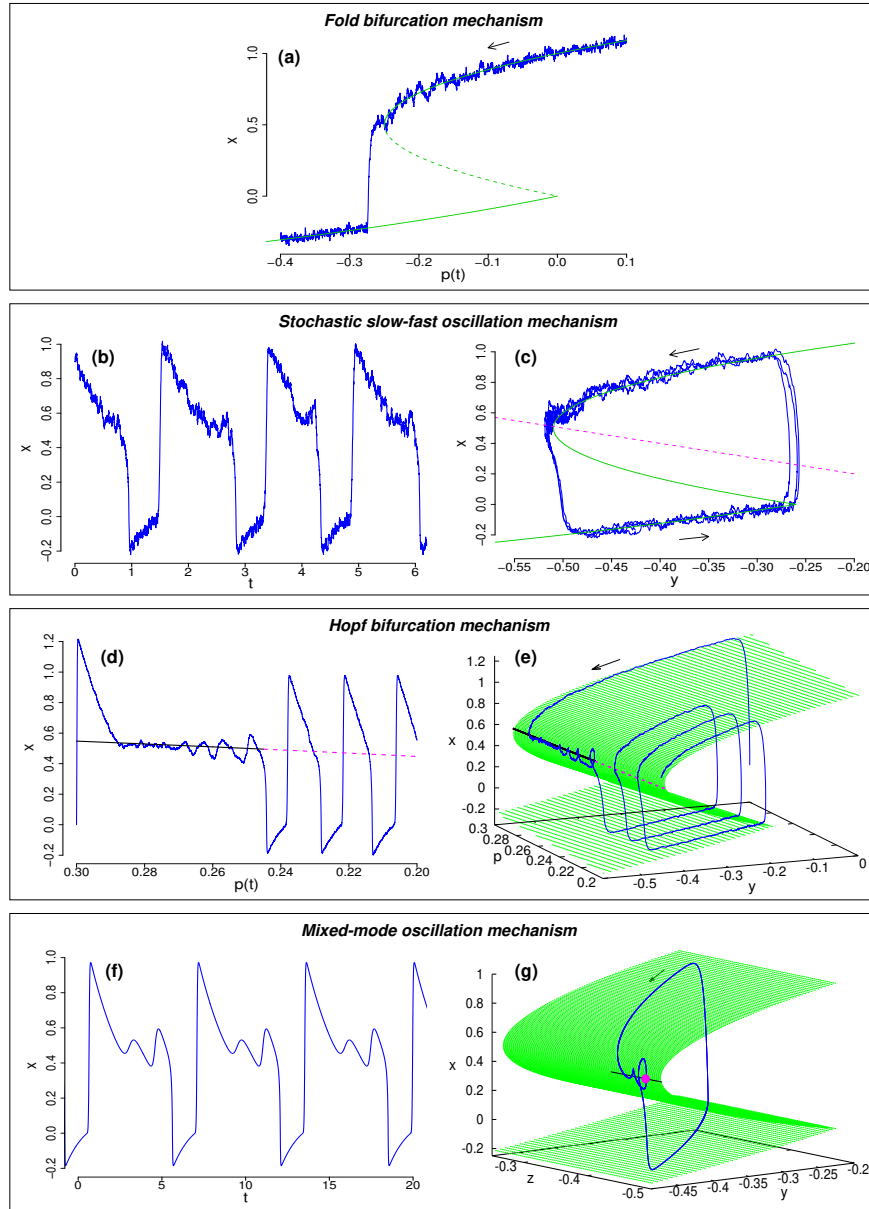


541 **Figure 3.** Same as Fig. 2 but for the following 6 interstadials, from 74 ka to 12 kyr b2k.



542 **Figure 4.** Detection of precursor signals of DO cooling transitions for different interglacials, dif-
 543 ferent proxy variables, different ice cores, and different CSD indicators. (a,b) Robustness analysis
 544 of precursor signals with respect to the smoothing span and the rolling window size (% of inter-
 545 stadal length): the case of GI-25 interstadial from the NGRIP $\delta^{18}\text{O}$ record. The CSD indicator
 546 is the variance in (a) and the lag-1 autocorrelation in (b). Cross marks (x) indicates statistically
 547 significant positive trend of the respective CSD indicator ($p < 0.05$) based on a phase surrogate test
 548 (Methods), small open circles (o) indicate barely significant positive trends ($0.05 < p < 0.1$) and

549 cells are left blank if $p > 0.1$. (c) Durations of interstadials longer than 1000 yr. (d) Robustness
550 of finding precursor signals for DO cooling transitions. The color indicates the number significant
551 ($p < 0.05$) positive trends in each of the 30 sets of the smoothing spans and the rolling window
552 sizes as in (a) and (b). For the cases of grey-shaded cells, the data is not publicly available.



553 **Figure 5.** Four potential dynamical mechanisms for the DO cooling transitions (Methods): (a) Fold
554 bifurcation mechanism. The time series $x(t)$ for decreasing $p(t)$ (blue). The green lines show the
555 stable (solid) and unstable (dashed) fixed points. (b,c) Stochastic slow-fast oscillation mechanism
556 of a FHN-type model. An example time series $x(t)$ is shown in (b) and the phase space trajectory
557 (blue) in (c); the x -nullcline, i.e., the critical manifold, is shown in green. The y -nullcline is shown
558 in dashed magenta. (d,e) Hopf bifurcation mechanism. An example time series $x(t)$ is shown in
559 (d) as a function of $p(t)$. Stable (black, solid) and unstable (magenta, dashed) fixed points are also
560 shown. The corresponding phase space trajectory $(x(t), y(t))$ for decreasing p is shown in (e) in
561 blue. The critical manifold (green). (f,g) Mixed-mode oscillation mechanism. An example time
562 series $x(t)$ is shown in (f) and the corresponding phase space trajectory in (g). The magenta dot
563 is the saddle point with a stable manifold in the direction of the black segment; the trajectory is
564 spiralling around it.